On contrast parameters and topographic artifacts in near-field infrared microscopy

D. V. Palanker,[a] D. M. Simanovskii, P. Huie, and T. I. Smith
Picosecond Free Electron Laser Center, W. W. Hansen Experimental Physics Laboratory, Stanford University, Stanford, California 94305

(Received 27 October 1999; accepted for publication 7 September 2000)

Near-field microscopy overcomes the diffraction limit through the partial conversion of the evanescent fields, formed around the subwavelength sources of light, into propagating waves by interactions between the probe and the sample. Contrast parameters in this imaging technique are quite different from those in conventional (far-field) optics. We study the mechanisms of image formation in the transmission mode of a near-field microscope in the mid-infrared part of the spectrum (6–10 μm). The amount of light propagating from a subwavelength aperture through a flat substrate (''allowed'' light) is found to strongly increase as the tip approaches the sample, generating topographic artifacts in near-field images. Such artifacts can be eliminated by flat sample preparation techniques. The transmitted power is strongly influenced by the refraction index of the sample resulting in a substantial difference of the near-field spectrum from the far-field one. A model describing tunneling of light through a subwavelength aperture into the substrate has been developed and is in very good agreement with the experimental data. The model predicts that spectral sensitivity is enhanced with smaller tip diameters. © *2000 American Institute of Physics.* [S0021-8979(00)09023-X]

I. INTRODUCTION

Infrared (IR: 5–12 μm) spectroscopy is a widely used sensitive technique for detection and characterization of molecules. Current biomedical applications of Fourier transform infrared (FTIR) microspectroscopy include identification of tumor cells[1] and bacteria,[2] mapping of calcified atherosclerotic plaques[3] and brain tissue,[4] finding foreign material in tissue,[5] etc. In these applications spatial resolution is typically limited to about 25–50 μm due to either imperfection of the imaging optics or the beam quality of the IR source. Highly collimated beams from synchrotron radiation allow for achieving a diffraction limited resolution,[6] namely one wavelength with the objective of 0.6 NA. This resolution was already sufficient to attempt imaging of protein and lipid distribution in large (20 μm) cells.[6]

For further improvement of the spatial resolution a scanning near-field optical microscopy has been developed that provides subdiffraction-limited resolution using a subwavelength size source (or collector) of radiation which is raster scanned over the sample surface at small (several nanometers) distance.[7] As a light source (or collector), very fine tapered fiber tips are generally used, coated with a thin layer of metal to prevent light leakage except at the very end of the tip where there is a small aperture. In the mid-IR part of the spectrum resolution of $\lambda/4$ (namely 1 μm at $\lambda = 4$ μm[8] and 2 μm at $\lambda = 8$ μm[9]) has been demonstrated. In addition to the subwavelength resolution, this approach allows for underwater imaging of thin samples (living cells, for example, Ref. 9) which is problematic with conventional FTIR microscopes due to strong water absorption of the IR radiation.

Strong attenuation of light in the subwavelength part of the tapered fiber (10^{-6}–10^{-4} typically[10]) together with heating of the fiber coating by light[11] limit the output signal and, consequently, the size of the aperture. To overcome these limitations, apertureless schemes have been developed which are based on detection of light scattered from oscillating tapered metal tips.[12,13] Features smaller than 100 nm have been imaged at 10.6 μm wavelength (CO_2 laser).[14,15] This approach, based on a lock-in detection of the signal, requires continuous (or at least ms-long pulsed) lasers. Due to the lack of convenient continuous sources of tunable mid-IR radiation, suitable for purposes of spectroscopy, we explore a fiber-based approach to near-field imaging and spectroscopy utilizing pulsed IR lasers.

Contrast parameters in various modes of the near-field microscopy (transmission, reflection and scattering) may be very different from those of conventional (far-field) microscopy. Although this issue has attracted growing attention in recent years,[16–18] the mechanisms of image formation are not yet well understood, and different contrast parameters have been claimed by various researchers using similar techniques.[13,15] In the present work we study the contrast parameters in transmission mode (fiber-based) near-field microscopy, including the influence of the sample and substrate refraction indices, as well as the role of sample topography in near-field image formation.

II. EXPERIMENTAL SETUP

A. Near-field probe

Our experiments have been performed in two spectral regions: 6–7 μm, and 9.2–10.7 μm using the Stanford Picosecond Free Electron Laser (FEL) and a pulsed grating-

[a]Electronic mail: palanker@stanford.edu

stabilized CO_2 laser (J48G-1W-36, Synrad Inc. Mukilteo, WA), respectively. Chalcogenide glass fibers (Amorphos Materials Inc., Garland, TX) with a 100 μm core were used to deliver the infrared radiation to a metal-coated tapered tip with a subwavelength opening at the apex, which served as a near-field probe. Sharp tips (radii of curvature at the apex were less than 1 μm) were produced by chemical etching in Piranha solution (7:3 mixture of concentrated sulfuric acid and 30% hydrogen peroxide).[19] These tips were completely coated with gold (150 nm thickness) by vacuum evaporation, and the level of residual leakage of light from the tip was measured using a liquid nitrogen-cooled mercury cadmium telluride (MCT) detector (KMPV50-.5-J2, Kolmar Technologies Inc., Phoenixville, PA). Only tips with a leakage level bellow the detectable threshold (2 nW) were selected. They were mounted on a piezo scanning stage (NSOM 100, Nanonics Inc., Jerusalem, Israel), positioned on an inverted microscope (Axiovert 35, Zeiss Inc.), and scanned across fine polishing paper (0.05 μm grain size) until a detectable IR signal appeared. Measurements performed with a scanning electron microscope have shown that a typical aperture size was about 1 μm. This method enabled us to create high quality optical probes with a light source well localized at the apex of the tip.

B. Positioning of the probe

Sheer force feedback was employed for control of the distance between the tip and the sample. The optical probe was mounted on one arm of a standard 32 768 Hz tuning fork. With the probe attached the resonance frequency was shifted typically to 32 kHz and the quality factor was about 300. The tuning fork was driven by a 10 mV sinusoidal signal at the resonance frequency. Current in the circuit was detected by a lock-in amplifier (EG&G, model 5210) and used to control the feedback system (SPM100, RHK Technologies, Rochester Hills, MI). This technique allowed us to maintain the distance between the tip and the sample with a precision of a few nanometers.

To ensure that optical detection conditions would be constant during scanning, the probe was fixed at the focus of the IR objective and the sample was moved (see Fig. 1). The vertical axis of the three-dimensional piezo scanning stage was used to maintain contact with the probe, while the *X* and *Y* axes were used for lateral scanning. The scanning rate was determined mainly by the feedback response time, and it took typically 10 s per line of 128 pixels.

C. Optical setup

The near-field microscope used in our experiments was mounted on an inverted optical microscope, so that the sample could be observed using transmitted as well as reflected light, allowing for precise positioning of objects with respect to the near-field probe. Radiation transmitted through the sample and the substrate was collected with a reflective objective (50×, NA 0.45, Ealing Inc.) and registered by a MCT detector positioned in the focal plane of the objective. In this configuration only the small part of the optical probe close to the apex was imaged on the detector's sensitive area

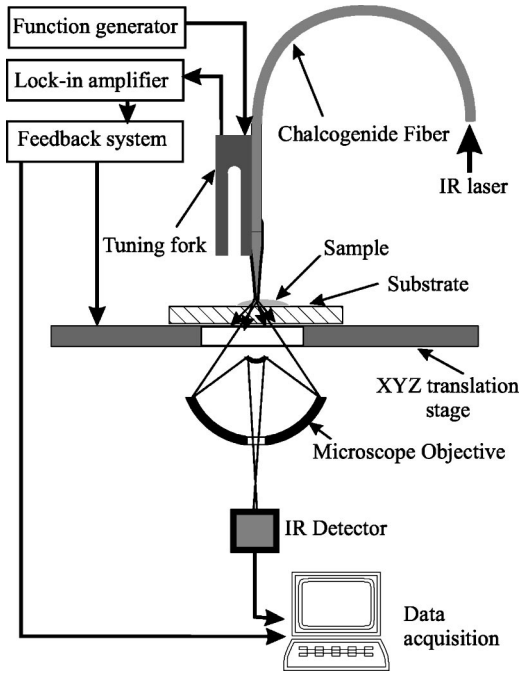

FIG. 1. Schematic representation of the illumination-mode near-field microscope built on a conventional inverted microscope with a sheer force-based feedback system.

(0.3×0.3 mm) providing a strong suppression of any background radiation which might originate from imperfections in the gold coating of the optical probe.

D. Sample preparation

To investigate contrast parameters and mechanisms of near-field image formation, objects with well-known optical properties and simple geometrical shapes were chosen. Most of the measurements were performed with polystyrene droplets deposited onto a calcium fluoride substrate. Standard polystyrene beads with 1 and 3 μm diameters were deposited onto the substrates from a water suspension. The balls were fixed on the substrate by heating it to a temperature slightly in excess of the softening temperature of polystyrene (~100 °C). The resulting structure appeared to be a set of single polystyrene droplets with a diameter slightly exceeding the initial diameter of the beads (due to flattening). In addition to the calcium fluoride (refraction index $n=1.3$), gallium phosphate ($n=3.0$) and germanium ($n=4.0$) substrates were tested as well.

III. EXPERIMENTAL RESULTS AND PHENOMENOLOGICAL MODEL

A. Approach curves

Subdiffraction limited resolution in near-field microscopy results from the interaction of the nonpropagating electromagnetic field generated around the probe with the sample.[20] Since the evanescent fields decrease rapidly with distance (on the order of a tip diameter), this interaction depends strongly on the separation between the near-field probe and the sample. Thus the sample topography is heavily involved in the near-field image formation.

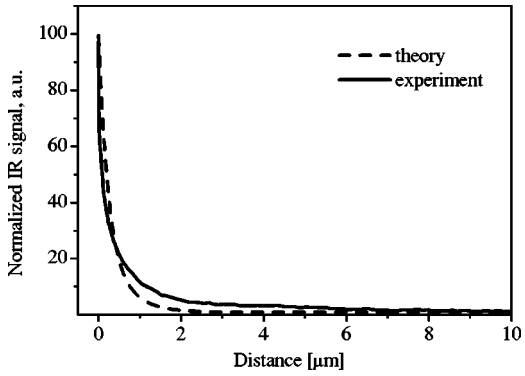

FIG. 2. Approach curve measured on a hemispherical silicon substrate at 9.3 μm wavelength with tip diameter of 0.8 μm. The dashed line represents model calculations.

The most direct way to characterize the influence of topography on the near-field signal is to measure approach curves, i.e., transmitted IR signal versus the distance between the probe and the substrate. In order to distinguish between the ''allowed'' and ''forbidden'' light (i.e., light propagating inside the substrate at the angles below and above, respectively, of the total internal reflection angle on the substrate/air interface) we performed measurements on two types of substrates. The first was a flat silicon wafer with parallel surfaces which transmits only the allowed component, while the second had a flat upper surface and a hemispherical bottom which allowed for detection of both the allowed and the forbidden components of the total signal. Approach curves measured on these substrates ($n=3.4$) with a tip diameter of 0.8 μm at a wavelength of 9.3 μm and normalized to the far-field signal (large separation between the tip and the substrate) are shown in Figs. 2 and 3. The signals rapidly increase as the separation between the tip and the substrate becomes smaller than ~ 0.5 μm and reach the levels of 100 ± 5 for the total signal (hemispherical substrate) and 4 ± 0.2 for its allowed component (flat substrate).

B. Theoretical model

In an attempt to characterize quantitatively the near-field signal as a function of the tip diameter, tip-sample separation, and the sample index of refraction, we have developed

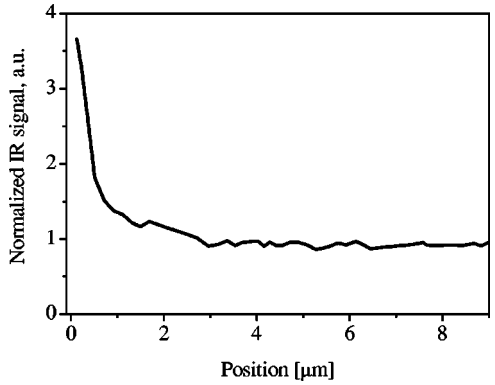

FIG. 3. Approach curve measured on a flat silicon substrate at 9.3 μm wavelength using tip of 0.8 μm diameter.

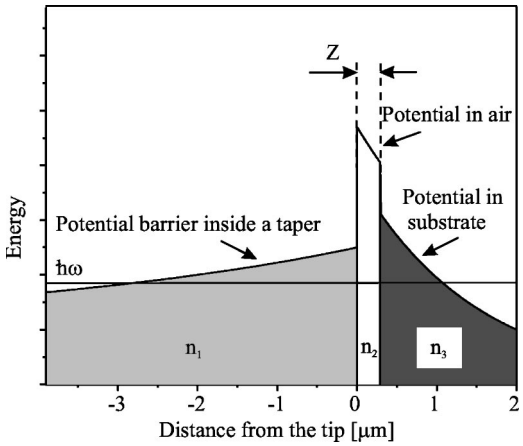

FIG. 4. Schematic representation of the potential barrier for photons in the subcutoff part of the taper, and its penetration into air and the substrate to the depth of the ''formation length'' of the propagating wave. Z is the width of the air gap between the probe and the substrate.

a phenomenological model which describes the experimental situation as one-dimensional photon tunneling from the fiber through the ''forbidden zone'' of the subwavelength taper into the substrate. It is not unusual to consider photon propagation through subwavelength structures as quantum tunneling,[21,22] but since there is no unambiguous potential which can be assigned to the photon, any particular case requires certain assumptions and has its own limitations.

The diagram of the potentials used in our model is shown in Fig. 4. The potential barrier related to the penetration of light through the subwavelength tapered fiber tip can be considered as being formed of two components: barrier in the subcutoff region of the taper, and a barrier corresponding to emission from the subwavelength aperture. The tunneling probability can be written in the form

$$T\propto \exp\left(-\int_{z\,\min}^{Z_{\max}}\sqrt{U(z)^2-\left(\frac{B}{\lambda}\right)^2}\,dz\right), \tag{1}$$

where $U(z)$ is a potential, B/λ represents the photon energy, $Z_{\min}, Z_{\max}$ are the ends of the barrier, where $U(z_{\min})=U(z_{\max})=B/\lambda$.

Attenuation of the field inside the taper is determined by the imaginary part of the wave vector in axial direction[23]

$$\begin{aligned} &k_z=\sqrt{k_0^2-k_T^2},\\ &T\propto \exp\left(iC\left(\int_{z_1}^{z_2}\sqrt{k_0^2-k_T^2}\,dz\right)\right), \end{aligned} \tag{2}$$

where k_0 is the photon wave number, and k_T is the transverse component. The imaginary part of k_z is nonzero in the area where $k_T>k_0$. Inside the taper k_T is reciprocal to the diameter of the waveguide,[23] thus transmission through the subcutoff taper can be expressed as the following:

$$T\propto \exp\left(iC\int_{z_1}^{z_2}\sqrt{k_0^2-\left(\frac{A}{n_1\cdot d(z)}\right)^2}\,dz\right). \tag{3}$$

This allows one to assign each point of the tapering zone a certain potential, which is a function of the taper diameter $d(z)$ and n_1, the index of refraction of the fiber

$$U(z)=\left(\frac{A}{n_1\cdot d(z)}\right),\quad \text{for}\quad z<0.$$

The second part of the photon path—the subwavelength zone to the right of the aperture—represents another obstacle. Since a propagating wave cannot exist in a subdiffraction limited volume, we assume that the photon will experience the potential barrier not only within the plane of the aperture, but also behind it, until the wave extends in space to dimensions above the diffraction limit. Since the width of the spherical wavefront extends linearly with its radius, the height of the potential barrier will scale reciprocally with the distance from the aperture. Thus for the area to the right of the aperture ($z>0$) we can describe the potential in the following way:

$$U(z)=\left(\frac{A}{n\cdot(z+d)}\right),$$

where $n(z)$ is the refraction index of the media outside the fiber and A is a constant, which will be determined below. Since in all our experiments only the conditions outside the fiber have been varied, and all measurements were normalized to the signal emitted from the free standing fiber in the air, we are interested only in the potential corresponding to positive values of z. In this case we can consider the field intensity ''delivered'' to the aperture through the tapered zone as a constant and rewrite the expression for the probability of tunneling in the following way:

$$T\propto \exp\left(-\int_0^{z_{\max}}\sqrt{\left(\frac{A}{n(z)\cdot(z+d)}\right)^2-\left(\frac{B}{\lambda}\right)^2}\,dz\right),\qquad (4)$$

where $z_{\max}$ is a distance at which barrier height becomes equal to the photon energy. Since $n(z)$ is either constant over all the integration region (homogeneous media), or has constant values over certain z intervals (e.g., air gap between the tip and the substrate), such an indefinite integral can be easily taken analytically for each interval with constant n

$$T\propto\exp\left(-\frac{A}{n}\left[\sqrt{1-a^2}+\frac{1}{2}\ln\frac{1-\sqrt{1-a^2}}{1+\sqrt{1-a^2}}\right]\right),\qquad (5)$$

where $a=d\cdot B\cdot n/(A\cdot\lambda)$. In order to determine the parameter A we apply the model to a situation that has an exact analytical solution—a flat screen with a small hole illuminated by a plane wave. In this case the intensity of radiation transmitted through a subwavelength hole with diameter d in vacuum ($n=1$) is proportional to $d^2\cdot T$, which in the limit of $d\ll\lambda$ reduces to d^{2+A}/λ^A. To match the scaling law based on Bethe's solution of this problem[24,25] A should be equal to 4.

Ratio $A\cdot\lambda/B$ in our model actually determines the boundary at which photon becomes free. This value should be close to the diffraction limit ($A/B\approx 0.5$). Still, it is a parameter, which can be used to optimally fit experimental approach curves. Expression (5) corresponds to the experimental situation with a hemispherical substrate, where the radiation once emitted into the material can leave it experiencing only normal incidence reflection losses on the spherical surface. Fitting the approach curve measured on silicon hemispheres with model calculations [Fig. 2] provides a ratio $A/B=0.4$, which is close to the expected diffraction limit value.

All the expressions presented above have been obtained for the total signal that consists of the allowed and forbidden components (i.e., the light propagating inside the substrate under the angles which are smaller and larger, respectively, than the angle of total internal reflection). In order to distinguish between the allowed component and the total signal (in the case of a flat substrate) one has to take into account the angular distribution of the radiation. The emission pattern of an aperture changes from a dipole-like one (at $d\ll\lambda/n$)[24,26] to a pattern corresponding to the divergence of the input beam, when the diameter of the aperture is larger than the cutoff diameter. Introducing this dependence into our calculations we found that even for allowed light (i.e., the light transmitted through a flat substrate) there is still a considerable enhancement of near-field signal which is in good agreement with our experimental data [Figs. 3, 5(a), and 5(b)].

C. Refraction index and wavelength dependence

Figure 5 displays the ratio of the IR transmission measured when the tip was held in contact with substrate to the signal measured when the tip was withdrawn from the near-field (extreme positions on the approach curves). This ratio was measured first with Ge substrate ($n_3=4$, $d=1$ μm) as a function of the wavelength from 9.2 to 10.7 μm [see Fig. 5(a)]. The curve through the data was calculated using the parameters determined above. It fits the experimentally measured values remarkably well.

In the next experiment we used a constant wavelength (9.7 μm) and changed the substrates. These data, shown in Fig. 5(b), also fit the model (see curve corresponding to $d=1$ μm). At relatively low indices ($n_3<2$) the rise in the near-field transmission is mostly determined by the tunneling effect. At higher indices the tunneling effect saturates (slope changes around $n_3=2$) and the loss due to reflection on the air/substrate interface in the far field contributes the most to the change of the near-/far-field ratio. With smaller tip diameters [$d=0.6$ and 0.3 μm in Fig. 5(b)], the index dependence becomes steeper, and tunneling saturation is shifted towards higher refraction index values.

D. Near-field spectroscopy

The strong dependence of the near-field emission on the refraction index of the sample (much stronger than just reflection loss, especially at low indices) leads to a substantial difference between a near-field transmission spectrum and a conventional (far-field) absorption spectrum. This difference was demonstrated using a thin (0.5 μm) polymer film (epoxy resin LX112). The Stanford FEL was used as a source of tunable mid-IR radiation. The near-/far-field ratio measured with 1 μm tip as a function of wavelength is plotted in Fig. 6(a). A FTIR absorption spectrum (dashed line 1) and calculations based on our model (solid line 2) are shown for comparison in the same figure. As expected, the near-/far-field ratio is related to the absorption spectrum in a derivative-like

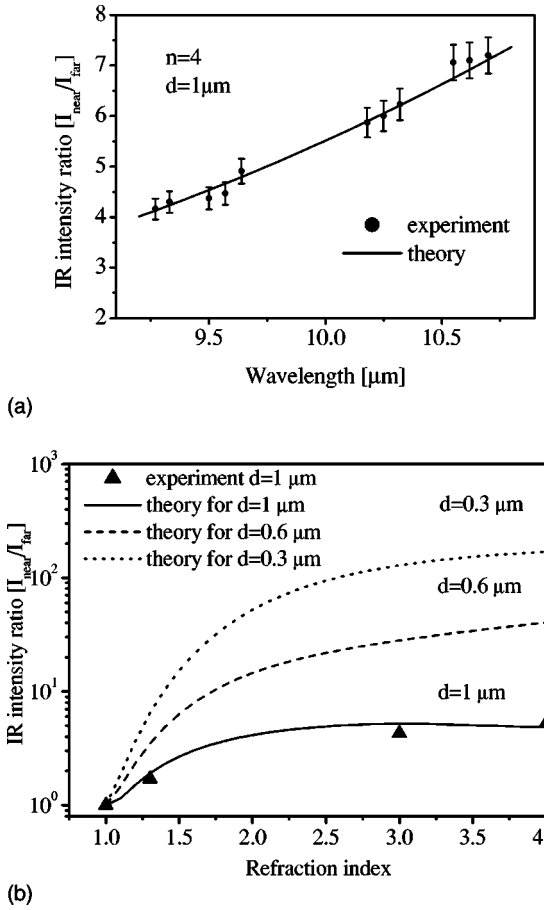

FIG. 5. (a) Near-field/far-field ratio measured on a flat Ge substrate with 1 μm tip as a function of wavelength. The solid line represents calculations based on the tunneling model. (b) Near-/far-field ratio as a function of refraction index measured and calculated for a Ge substrate at 9.5 μm. Symbols are experimental points. Solid lines represent calculations for various tip diameters.

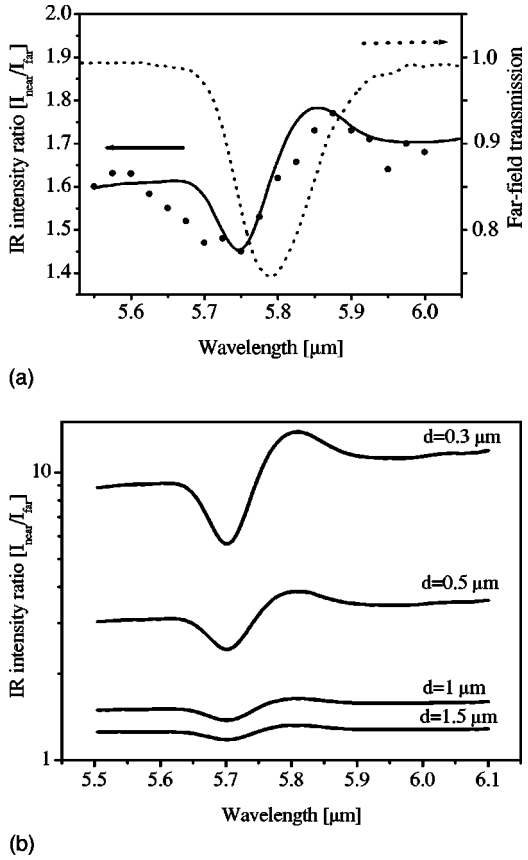

FIG. 6. (a) Near-field spectroscopy. Symbols and a solid line representing experimental data and calculations for the near-/far-field ratio obtained with 1 μm tip on 0.5-μm-thick epoxy resin (LX112) film (scale shown on the left). The dashed line is a FTIR absorption spectrum of the same sample (scale shown on the right). (b) Near-field spectra of the same sample calculated for various tip diameters. Note the semilogarithmic scale of intensity.

fashion, since the real and imaginary parts of the refraction index are linked by the dispersion (Kramers–Kronig) relations. The nonzero slope of the base line in solid curve results from the wavelength dependence of the near-field tunneling [similar to that shown in Fig. 5(a)]. As already shown in Fig. 5(b), the sensitivity of this mode of the near-field spectroscopy (near-/far-field ratio measurement) strongly depends on tip diameter. In Fig. 6(b) four spectra are shown, calculated for the same polymer film and tip diameters ranging from 1.5 to 0.3 μm. These calculated spectra demonstrate the increased amplitude of modulation of the near-/far-field ratio at decreasing tip diameters. The near-field spectral sensitivity is enhanced as compared to conventional absorption spectrum approximately by the ratio of the light penetration depth to the size of the near-field zone.

IV. IMAGING

Typical topographic and near-field optical images of a 1 μm polystyrene droplet ($n=1.45$) on a CaF_2 substrate are shown in Fig. 7. The image appears to be about 2 μm in diameter since it represents a convolution of the object and of the probe, each of which were 1 μm in diameter. The near-field image consists of two bright segments of a ring surrounding the edge of the droplet, and an area inside the boundaries of the droplet that appears darker than the background. A typical image of a 3 μm droplet (taken with another tip of the same diameter) shown in Fig. 8 is quite different. In addition to the same bright ring outside the topographic boundary, it has a dark ring inside the boundary, and a central part of the droplet which is brighter than the background.

The complexity of the image is due to the influence of the sample topography. The evanescent field confined near the aperture interacts with an object when the tip is positioned in close proximity to it, thus resulting in formation of an external ring (position 2 in Fig. 9). The dipole character of the ring can be plausibly explained by the fact that the aperture is illuminated by plane polarized light.[27] An asymmetry of the tip (nonround shape) may explain the uneven brightness of the two segments. When the tip starts climbing onto the sample, touching it by its edge (position 4), the distance between the aperture and the substrate increases, resulting in a decrease in the amount of outcoupled radiation. This leads to the formation of the dark area inside the topographic boundaries of the sample. On top of the ball the distance between the aperture and the material becomes small again (position 3). As discussed above, outcoupling of light from the fiber is very sensitive to its separation from the sample. It

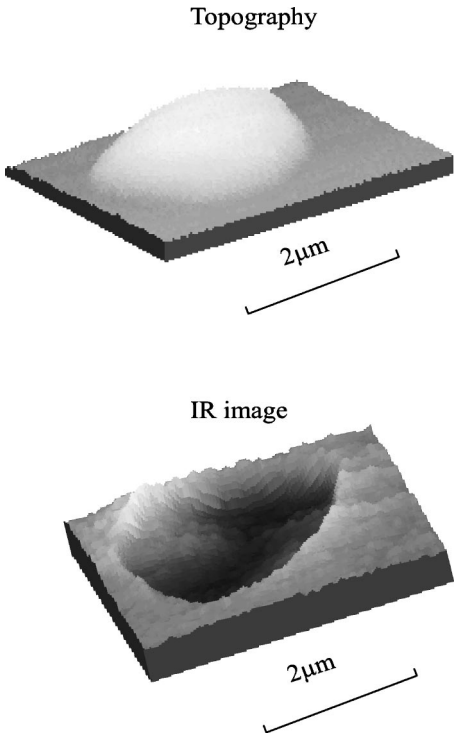

FIG. 7. Three-dimensional representation of the topographic (top) and near-field optical images of a 1 μm polystyrene ball on a CaF_2 substrate (bottom).

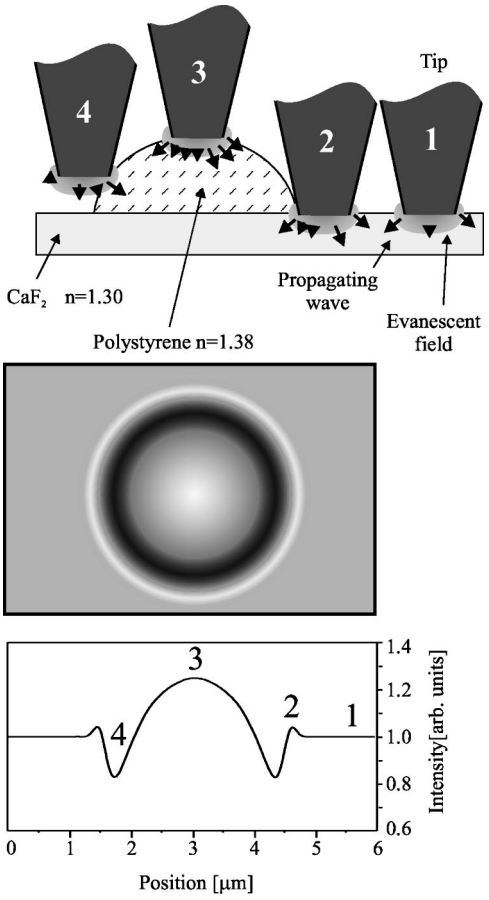

FIG. 9. Schematic diagram illustrating the mechanisms of bright and dark ring formation in near-field imaging of a hemisphere.

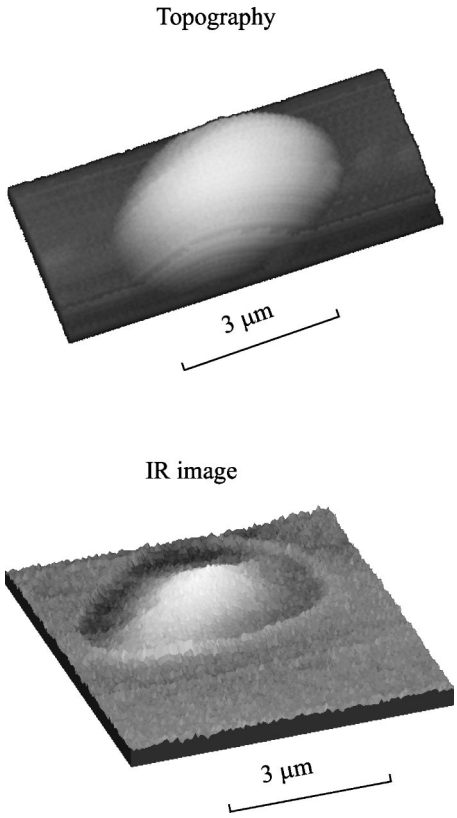

FIG. 8. Three-dimensional representation of the topographic (top) and near-field optical images of 3 μm polystyrene balls on a CaF_2 substrate (bottom).

occurs efficiently when the near-field zone is ''filled'' with material (i.e., the sample's radius of curvature is large enough to provide a good ''optical'' contact for tunneling). Depending on such things as whether the refraction index of the sample is higher than that of the substrate, and/or if the sample fills the near-field zone better than the substrate, the object will appear brighter or dimmer than the background. (Poor optical contact between the tip and the substrate may result from polishing or positioning of an aperture plane at some angle to the substrate resulting in their separation.)

The influence of the substrate on near-field image formation (resulting from variation of the distance between the probe and the substrate due to the sample topography) can be prevented if the scanning is performed in a ''constant height mode''—at constant separation between the probe and the substrate. Typically, the drift of the tip during scanning does not allow turning off the feedback mechanism, so we accomplished this mode of scanning using a special ''flat'' sample preparation. The samples (3 μm polystyrene balls) were positioned on the lower side of a thin (100 nm) nitrocellulose film, and images were collected through that film with a 1 μm tip scanned in contact with the film. Since the distance between the probe and the substrate (nitrocellulose film) was constant during the scanning, the image, shown in Fig. 10, represents only the contribution of the sample, with no topographic artifacts. For comparison, see in Fig. 8 a picture of similar object imaged from above, when it was positioned on

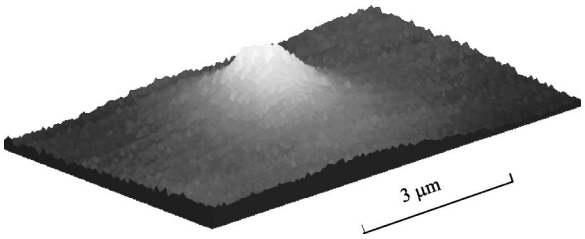

FIG. 10. Three-dimensional representation of the image of a 3 μm polystyrene ball obtained through a 0.1 μm polymer film with a 1 μm tip at 10.7 μm wavelength. Note the absence of topographic artifacts (dark ring) typical for images of similar objects positioned on a CaF_2 substrate (Fig. 8, bottom frame).

a thick CaF_2 substrate, and the tip was following its topography. A strong artifact—a dark ring within topographic boundaries of the ball—is obvious in this picture.

V. CONCLUSIONS

Transmission of light through a subwavelength tapered fiber tip into a sample depends strongly on the probe-sample separation and on its index of refraction. This effect can provide unique information on the material structure at a subwavelength scale, but it can also introduce strong topographical artifacts into the image. These artifacts result from variations in the distance between the probe and the substrate that supports the sample during scanning. Such effects can be eliminated using flat sample preparation techniques.

A phenomenological model of photon tunneling from the near-field probe into the substrate has been developed, and is in good agreement with our experimental data. The strong dependence of near-field transmission on the refraction index of the sample results in the substantial difference between near-field and far-field spectra. The model predicts that the sensitivity of near-field spectroscopy is enhanced relative to conventional absorption-based measurements by the ratio of the light penetration depth to the size of the near-field zone.

ACKNOWLEDGMENTS

This work was supported by the Office of Naval Research, Grant No. N00014-94-1-1024, by the National Science Foundation, Grant No. DBI-9819778, and by Department of the Air Force, Grant No. F49620-00-1-0349.

[1] P. T. T. Wong, R. K. Wong, T. A. Caputo, T. A. Godwin, and B. Rigas, Proc. Natl. Acad. Sci. U.S.A. **88**, 10988 (1991). P. T. T. Wong, R. K. Wong, and M. F. K. Fung, Appl. Spectrosc. **47**, 1058 (1993).
[2] D. Naumann, S. Keller, D. Helm, C. Schultz, and B. Schrader, J. Mol. Struct. **347**, 399 (1995); D. Naumann, D. Helm, and H. Labischinski, Nature (London) **351**, 81 (1991).
[3] R. Manoharan, J. J. Baraga, R. P. Rava, R. R. Dasari, M. Fitzmaurice, and M. Feld, Atherosclerosis (Berlin) **103**, 181 (1993); D. R. Kodali, D. M. Small, J. Powell, and K. Krishnan, Appl. Spectrosc. **45**, 1310 (1991).
[4] S. M. LeVine and D. L. Wetzel, Appl. Spectrosc. Rev. **28**, 385 (1993).
[5] J. A. Centeno, V. F. Kalasinsky, F. B. Johnson, T. N. Vinh, and T. J. O'Leary, Lab. Invest. **66**, 123 (1992).
[6] N. Jamin *et al.*, Proc. Natl. Acad. Sci. U.S.A. **95**, 4837 (1998).
[7] See, for example, M. A. Paesler, *Near-Field Optics: Theory, Instrumentation, and Applications* (Wiley, New York, 1996).
[8] A. Piednoir, C. Licoppe, and F. Creuzet, Opt. Commun. **129**, 414 (1996).
[9] M. K. Hong, A. G. Jeung, N. V. Dokholyan, T. I. Smith, H. A. Schwettman, P. Huie, and S. Erramilli, Nucl. Instrum. Methods Phys. Res. B **144**, 246 (1998).
[10] D. Zeisel, S. Nettesheim, B. Dutoit, and R. Zenobi, Appl. Phys. Lett. **68**, 2491 (1996); L. Novotny, D. W. Pohl, and B. Hecht, Opt. Lett. **20**, 970 (1995).
[11] M. Stahelin, M. A. Bopp, G. Tarrach, A. J. Meixner, and I. Zschokke-Granacher, Appl. Phys. Lett. **68**, 2603 (1996).
[12] A. Larech, R. Bachelot, P. Gleyzes, and A. C. Boccara, Opt. Lett. **21**, 1315 (1996).
[13] F. Zenhausern, Y. Martin, and H. K. Wickramasinghe, Science **269**, 1083 (1995).
[14] B. Knoll and F. Keilmann, Appl. Phys. A: Mater. Sci. Process. **66**, 477 (1998).
[15] B. Knoll and F. Keilmann, Nature (London) **399**, 134 (1999).
[16] L. Novotny, J. Opt. Soc. Am. A **14**, 91 (1997); B. Hecht, H. Bielefeldt, D. W. Pohl, L. Novotny, and H. Heinzelman, J. Appl. Phys. **84**, 5873 (1998).
[17] P. J. Valle, J. J. Greffet, and R. Carminati, J. Appl. Phys. **86**, 648 (1999); C. E. Jordan, S. J. Stranick, L. J. Richter, and R. R. Cavanagh, J. Appl. Phys. **86**, 2785 (1999); S. I. Bozhevolnyi, I. I. Smolyaninov, and O. Keller, Appl. Opt. **34**, 3793 (1995).
[18] B. Dragnea, J. Preusser, W. Schade, and S. R. Leone, J. Appl. Phys. **86**, 2795 (1999).
[19] M. A. Unger, D. A. Kossakovski, R. Kongovi, J. L. Beauchamp, and D. V. Palanker, Rev. Sci. Instrum. **69**, 2988 (1998).
[20] M. A. Paesler and P. J. Moyer, NSOM Imaging Theory, in *Near-Field Optics. Theory, Instrumentation, and Applications* (Wiley, New York, 1996), pp. 67–96.
[21] O. Keller, Phys. Rev. A **60**, 1652 (1999).
[22] C. Girard, Phys. Rev. B **58**, 12551 (1998).
[23] T. R. Corle and G. S. Kino, in *Confocal Scanning Optical Microscopy and Related Imaging Systems* (Academic, San Diego, CA, 1996), pp. 206–211.
[24] J. D. Jackson, in *Classical Electrodynamics*, 2nd ed. (Wiley, New York, 1975), pp. 407–415.
[25] H. A. Bethe, Phys. Rev. **66**, 163 (1944).
[26] C. Obermuller and K. Karrai, Appl. Phys. Lett. **67**, 3408 (1995).
[27] E. Betzig, J. K. Trautman, J. S. Weiner, T. D. Harris, and R. Wolfe, Appl. Opt. **31**, 4563 (1992).